ACCSCIENCE PUBLISHING

International Journal of Bioprinting

RESEARCH ARTICLE

Tiny bricks for oral bioprinting: Exploring gingiva and dental pulp-derived organ building blocks

Lidiia R. Grinchevskaia[1†], Anna V. Kardosh[1†], Vitalia R. Izhbulatova[1†], Nastasia V. Kosheleva[1], Daria S. Kuznetsova[1], Artem M. Mozherov[1], Yuri M. Efremov[1], Alexey L. Fayzullin[1], Polina Y. Bikmulina[1], Svetlana L. Kotova[1], Anastasia I. Shpichka[1], Oleg O. Pavlov[2], Boris P. Yakimov[1,2], and Peter S. Timashev[1*]

[1]Institute for Regenerative Medicine, I. M. Sechenov First Moscow State Medical University, Moscow, Russia

[2]Faculty of Physics, M. V. Lomonosov Moscow State University, Moscow, Russia

(This article belongs to the Special Issue: *Biofabrication Breakthroughs: Innovation and Application in Bioprinting, Biomaterials, and Organoid*)

Abstract

Today, organ building blocks (OBBs) serve as important tools for in vitro tissue modeling, personalized medicine, and regenerative approaches. Despite substantial advances in dental reconstruction methods, tissues of the oral cavity remain challenging to regenerate due to their complex structure and microenvironment. However, effective regeneration of the periodontal complex, e.g., in diseases such as periodontitis, persists, as current methods do not achieve complete tissue restoration. Cells from the gingiva and dental pulp are accessible sources of mesenchymal stem cells with high regenerative potential, making them promising materials for creating OBBs. These cells can serve as fundamental units for restoring the periodontal complex using techniques such as 3D bioprinting. This study aims to characterize and compare OBBs derived from gingival cells, pulp cells, and their combinations by assessing key parameters, including morphology, extracellular matrix composition, biomechanical properties, histology, and metabolic activity. Combining the two cell types improved the structural, mechanical, and functional properties of OBBs, making them more suitable for bioprinting than those derived from a single cell type. Moreover, all types of OBBs from the two cell cultures may be suitable as components of bioinks, depending on the specific purposes. The results provide insights into the potential use of these cell sources for tissue engineering and the development of personalized periodontal bio-constructs that may significantly improve treatment approaches for oral diseases.

Keywords: Organ building blocks; Tissue engineering; Regenerative medicine; Oral tissues; Gingiva cells; Dental pulp cells; Periodontal complex regeneration

†*These authors contributed equally to this work.*

***Corresponding author:**
Peter S. Timashev
(timashev_p_s@staff.sechenov.ru)

Citation: Grinchevskaia LR, Kardosh AV, Izhbulatova VR, *et al*. Tiny bricks for oral bioprinting: Exploring gingiva and dental pulp-derived organ building blocks. *Int J Bioprint*. 2026:12(2):026060050. doi: 10.36922/IJB026060050

Received: September 3, 2025

Revised: February 4, 2026

Accepted: February 5, 2026

Published online: February 19, 2026

1. Introduction

Periodontitis, a prevalent inflammatory disease, leads to the destruction of tooth-supporting tissues, including the alveolar bone, periodontal ligament, and cementum,

often resulting in tooth loss. Current regenerative therapies, such as bone grafts and barrier membranes, offer limited predictability, particularly for large or complex defects.[1] Consequently, there is a critical need for advanced bioengineering strategies that can recapitulate the hierarchical structure and function of the native periodontal complex.

Organ building blocks (OBBs) are 3D cellular structures capable of approximating some morphological and functional features of tissues and organs *in vitro*.[2] These units serve as fundamental modules for tissue engineering, regenerative medicine, and personalized drug screening. While this approach is established in models of the liver,[3] skin,[4] brain,[5,6] and intestine,[7] it is still gaining traction in dentistry. The current advances in 3D bioprinting for oral regeneration include the fabrication of porous scaffolds,[8,9] biocompatible composites,[10] vascular networks,[11] and models of tissue interfaces.[12] However, the specific use of pre-assembled, multicellular OBBs (rather than single-cell bioinks) to engineer the complex periodontal architecture remains a nascent area with high potential.

The oral cavity is a rich reservoir of accessible mesenchymal stromal cells (MSCs) with distinct regenerative properties.[13] To date, several types of oral stem cells have been identified: dental pulp stem cells,[14] stem cells from human exfoliated deciduous teeth,[15] periodontal ligament stem cells,[16] stem cells from the apical papilla,[17] dental follicle progenitor cells,[18] and gingiva-derived stem cells.[19] For this study, we selected dental pulp-derived cells and gingiva-derived cells for OBB formation based on their complementary and therapeutically relevant profiles.[20,21] This choice was motivated not only by their relative accessibility but also by the combination of biological properties most pertinent to the periodontal tissue engineering objectives. Pulp-derived cells possess a high potential for osteogenic differentiation,[22,23] making them strong candidates for the regeneration of hard tissues—alveolar bone and cementum. Gingiva-derived cells exhibit substantial immunomodulatory and anti-inflammatory properties,[24,25] which play a crucial role in modulating the inflammatory response and fostering a microenvironment conducive to soft tissue regeneration. We hypothesize that combining these two cell types within a single OBB creates a synergistic, multifunctional unit capable of concurrently promoting hard tissue formation and modulating the local immune response.

However, the functional output and structural integrity of any 3D construct, including OBBs, critically depend on the initial cell composition and the fabrication methodology.[26,27] Despite this conceptual promise, fundamental questions regarding the optimal formation, basic biophysical properties (e.g., morphology, compactness, and mechanical rigidity), and functional competence (e.g., viability and ingrowth capacity) of OBBs derived from gingival and pulp cells require further research.

Therefore, the aim of this study is to fabricate and characterize OBBs derived from human gingival and dental pulp cells. The specific objectives are to investigate: the basic characteristics of primary pulp-derived cell and gingiva-derived cell cultures; the influence of the fabrication method on the OBB morphology, compactness, and mechanical properties; and the functional potential of OBBs, as assessed through their viability and sprouting capacity.

2. Materials and methods

2.1. Isolation of primary cell cultures from oral cavity tissues using the explant method

Primary stromal cell cultures were isolated using the explant method from the samples of gingiva and dental pulp. This study used cells from three healthy donors (mean age 30 ± 5 years). Tissue samples were obtained from the Sechenov University Biobank; these samples were collected during tooth extraction procedures from healthy donors who had provided informed consent.

The tissue specimens were washed three times in a sterile Hank's balanced salt solution (HBSS; BioLoT, Russia) supplemented with a mixture of antibiotics, including gentamicin (60 μg/mL; Sigma-Aldrich, Germany), penicillin–streptomycin (penicillin 100 units/mL, streptomycin 100 μg/mL; Thermo Fisher Scientific, United States of America [USA]), and an antibiotic–antimycotic solution (1%; Sigma-Aldrich, Germany) for 5–10 min. After washing, the tissues were minced with a scalpel and scissors into small fragments. Using sterile forceps, tissue fragments were transferred into Petri dishes (Corning, USA) with a diameter of 35 mm, and a minimal volume (600 μL per dish) of complete culture medium was added to allow the explants to settle to the bottom and adhere to the plastic surface. The explants were cultured in a CO_2 incubator at 37 °C in a humidified atmosphere containing 5% CO_2, with repeated replacement of the medium.

Subsequently, migratory cells emerging from the tissue explants were carefully detached to prevent dislodging the explant. This was achieved by treating the cells three times with a 0.02% Versene solution (BioLoT, Russia), followed by one treatment with TrypLE™ (Gibco, USA). The cells were collected into a suspension, transferred into centrifuge tubes, and washed with HBSS. After centrifugation for 5 min at 300× g, the cell pellet was resuspended in the

complete culture medium and transferred into new Petri dishes for further cultivation.

2.2. Maintenance of cell cultures

Cell cultures were maintained in plastic-adherent Petri dishes in a CO_2 incubator at 37 °C in a humidified atmosphere containing 5% CO_2. The growth medium consisted of Dulbecco's modified Eagle medium (DMEM)/F12 (1:1) culture medium supplemented with *L*-glutamine and phenol red (BioLoT, Russia), along with 10% fetal bovine serum (FBS; Biosera, France), insulin–transferrin–selenium (ITS) supplement at a dilution of 1:100 (BioLoT, Russia), basic fibroblast growth factor (bFGF) at a final concentration of 10 ng/mL (PanEco, Russia), heparin at a concentration of 7.5 units/mL (Endofarm, Russia), and gentamicin up to a final concentration of 60 μg/mL (Sigma-Aldrich, Germany). Cells were monitored visually using an Axio Vert A1 inverted phase-contrast microscope (Carl Zeiss, Germany).

The cells were subcultured as they grew. To do this, the cultures were first treated three times with a 0.02% Versene solution, followed by one treatment with TrypLE. The cell suspension was transferred into a centrifuge tube, washed in HBSS, and centrifuged for 5 min at 300× g. The cell pellet was resuspended in a fresh culture medium and transferred to new dishes.

2.3. Flow cytometry

Gingiva- and pulp-derived stromal cells at passage 5 were characterized using MSC surface proteins as positive markers (cluster of differentiation [CD]44, CD90, CD73, CD105, and CD29) and hematopoietic and endothelial surface proteins as negative markers (CD31, CD19, CD11b, CD45, CD34, and human leukocyte antigen–D-related [HLA-DR]). For immunophenotyping, 1–2 × 10^6 cells were collected according to a standard protocol and centrifuged for 5 min at 300× g, after which the supernatant was removed. The cells were then washed with phosphate-buffered saline (PBS) and centrifuged again. The cell pellet was resuspended in the required volume of PBS containing 1% FBS, distributed into tubes (100 μL per tube), and stained with fluorochrome-conjugated antibodies (phycoerythrin [PE] or fluorescein isothiocyanate [FITC]) against CD44 (anti-CD44-PE), CD90 (anti-CD90-PE), CD73 (anti-CD73-PE), CD105 (anti-CD105-PE), CD29 (anti-CD29-PE), CD31 (anti-CD31-FITC), CD19 (anti-CD19-PE), CD11b (anti-CD11b-FITC), CD45 (anti-CD45-PE), CD34 (anti-CD34-PE), and HLA-DR (anti-HLA-DR-PE) (Miltenyi Biotec, Germany) at a ratio of 1:100 (1 μL antibody per 100 μL cell suspension). As an isotype negative control, mouse IgG1 antibodies conjugated with either PE or FITC were used. A cell suspension without antibody staining was applied as a negative control. Cells were incubated with the antibodies for 20 min at room temperature in the dark. After incubation, samples were centrifuged for 5 min at 1000×g, and the cells were resuspended in PBS. Surface marker expression analysis was performed on a Sony SH800S flow cytometer (Sony Biotechnology, USA) using a 488 nm laser, according to the manufacturer's protocol.

2.4. Preparation of agarose plates for organ building blocks formation

Agarose plates were prepared using 3D Petri dish silicone molds (Microtissues, USA). The molds were sterilized using UV irradiation in a bactericidal chamber (Microcid, Russia) for 15–20 min. Next, a 2% agarose solution was prepared in the DMEM/F12 medium supplemented with gentamicin (120 μg/mL). The solution was heated in a microwave oven and then poured into sterile silicone molds in aliquots of 500 μL. The agarose plates were further sterilized using UV irradiation in a laminar flow hood for 5–10 min. Once solidified, the plates were carefully removed from the molds, turned over, and again irradiated with UV light for 5–10 min. The agarose plates were stored at +4 °C in the DMEM/F12 medium supplemented with gentamicin up to 120 μg/mL.

2.5. Formation of organ building blocks

Agarose plates were additionally sterilized in a bactericidal chamber for 15–20 min. Sterile plates were transferred to a 12-well culture plate (Corning, USA). Cells were detached from culture flasks following a standard protocol and transferred to centrifuge tubes. A mixture of cells from three patients was used to form the OBBs. A 10 μL aliquot of the suspension was counted using a Neubauer chamber and centrifuged at 300× g for 5 min. After centrifugation, the supernatant was removed, and the cell pellet was resuspended in an appropriate volume of the complete culture medium to achieve the desired cell concentration. About 140 μL of the suspension was transferred to each agarose plate and left at +37 °C in a CO_2 incubator for 40–60 min to allow the initial cell aggregation. Afterward, wells of the culture plate were filled with the culture medium (~2 mL per well), and OBBs were cultured under standard conditions (+37 °C with 5% CO_2).

Two-layer OBBs were formed as follows: spherical aggregates ("cores") consisting of approximately 1,000 cells derived from either the gingiva or pulp tissue were generated according to the above protocol. After one day, the medium from the agarose plates containing the "cores" was carefully removed; then, about 140 μL of the cell suspension was added to each well. The plates were incubated at +37 °C with CO_2 for 40–60 min to allow initial

cell aggregation around the "cores." Subsequently, the wells were filled with the complete culture medium and cultured under standard conditions.

The culture medium was replaced every 2–3 days. OBBs were monitored visually using an Axio Vert A1 inverted light microscope with phase contrast (Carl Zeiss, Germany).

2.6. Morphological analysis of organ building blocks

Five experimental groups of OBBs (gingiva [G], pulp [P], 1:1 mixing gingiva- and pulp-derived cells [M], layering pulp–gingiva [PG], and layering gingiva–pulp [GP]) were obtained from three independent series. Samples were fixed in 10% neutral buffered formalin for 12 h. Half of the samples were placed in an O.C.T. cryogel (Sakura Finetek, USA) and sectioned with a Leica CM1520 cryostat (Leica Microsystems, Germany). Then, 5–7 μm-thick sections were stained with hematoxylin and eosin histological staining. The slides were digitized with a NanoZoomer S20MD scanner (Hamamatsu, Japan) for the morphological analysis. The second half of the samples was centrifuged and stained according to the protocol for visualization by microscopy with UV surface excitation (MUSE) method. Each sample was fluorescently stained with Hoechst 33258 (working concentration 50 μg/mL; B1155, Sigma-Aldrich, USA) dissolved in an eosin solution for 5 min. The optical system for MUSE imaging included three UV LEDs with a wavelength of 265 nm and a light microscope with 5×/0.15 NA and 10×/0.25 NA objectives (N-Achroplan, Carl Zeiss, Germany). The UV LEDs were fixated on a 3D-printed adapter. Fluorescent images were captured with a digital camera (AXIOCAM 506, Carl Zeiss, Germany).

2.7. Analysis of organ building block compactization and spreading dynamics

To assess the dynamics of OBBs' compactization, microphotographs were taken daily over a period of seven days using the built-in Axiocam 105 color camera (Carl Zeiss, Germany) and ZEN 2.6 lite software (Carl Zeiss, Germany). The measurements of OBBs' diameters were performed using the "Straight line" and "Measure" tools in the Fiji software.

For the analysis of spreading, OBBs were extracted from agarose plates and placed into centrifuge tubes; 10–20 OBBs were selected and transferred into wells of a six-well plate. Then, the wells were filled with a minimal volume of the culture medium to allow the OBBs to settle to the bottom and attach to the plastic. The OBBs were cultured under standard conditions (37 °C, 5% CO_2). To analyze the spreading dynamics, microphotographs were taken daily over 4 days using the built-in Axiocam camera 105 color (Carl Zeiss, Germany) and ZEN 2.6 lite software (Carl Zeiss, Germany). Cell spreading areas were measured using the "Freehand selections" and "Measure" tools in the Fiji software.

2.8. Immunocytochemical staining of 2D cultures and organ building blocks

For immunocytochemical (ICC) staining of 2D cultures, cells were seeded onto sterile coverslips at a density of 70,000 cells per slip. The next day, the coverslips with cells were washed with PBS and fixed in a 4% paraformaldehyde (PFA) solution (Sigma-Aldrich, Germany) for 30 min at 4 °C. After fixation, they were washed three times with PBS. For staining OBBs, they were extracted from agarose plates and transferred to centrifuge tubes; then, the culture medium was replaced with PBS for washing. The OBBs were fixed in 4% PFA overnight at 4 °C, followed by three washes with PBS.

After fixation, permeabilization was performed to improve the membrane permeability for antibodies by incubating the samples in a 0.2% Triton X-100 solution (PanReac AppliChem, Germany) in PBS for 10 min. Next, blocking was carried out to prevent nonspecific antibody binding by incubating the samples in a 10% FBS solution in PBS for 10 min. Then, primary antibody solutions prepared in PBS containing 10% FBS and 1% Tween 20 (Invitrogen, USA) were added. The following primary antibodies were used: anti-vimentin (1:1000; Ab 20346, Abcam, United Kingdom [UK]), anti-collagen I (1:500; Ab 34710, Abcam, UK), and anti-fibronectin 1 (1:500; PA5-99457, Invitrogen, USA). Cells and/or OBBs were incubated overnight at 4 °C. After the incubation with antibodies, samples were washed three times with PBS.

Secondary antibody solutions were prepared by adding secondary antibodies (1:500; Ab 150077, Abcam, UK; 1:500, Ab 150116, Abcam, UK) and/or Phalloidin-iFluor 594 Ab (176757, Abcam, UK) diluted at a ratio of 1:1,000 for actin filament staining. Samples with secondary antibodies were incubated at room temperature in the dark for 2 h, then washed twice with PBS. For visualization of nuclei, Hoechst 33258 dye solution was prepared at a working concentration of 2×10^{-3} mg/mL in PBS; stained samples were incubated in this solution for 30–40 min in darkness at room temperature. After staining, samples were washed with PBS and prepared for confocal microscopy.

2.9. Preparation of samples for confocal microscopy

For preparing samples of 2D cultures, a drop of ProLong™ mounting medium (Thermo Scientific, USA) was applied

to a glass slide, then a glass with cells was placed into it. Samples of OBBs in a small volume of PBS were placed onto a glass slide coated with poly-*L*-lysine (Thermo Scientific, USA). The excess liquid was removed from the slide, a drop of ProLong™ mounting medium was added, and the sample was covered with a coverslip. The prepared samples were stored at +4 °C. ICC staining was analyzed using an FW3000 laser-scanning confocal microscope (Olympus, Japan) at wavelengths of 405 nm, 488 nm, and 594 nm.

2.10. Measurement of organ building block stiffness by parallel plate compression testing

The mechanical properties of OBBs were analyzed via parallel-plate compression testing using the Microtester G2 (CellScale, Canada) micromechanical testing system. The measurement parameters were set as follows: compression limit at 50% of the original height of the OBBs; compression duration at 20 s; hold time in compressed state at 20 s; recovery time after compression at 20 s; and upper plate movement speed at 3 μm/s. OBBs were extracted from agarose plates and transferred into centrifuge tubes. The working chamber of the device was filled with PBS, and OBBs were placed on its platform. Using the control panel in the software, the upper plate was positioned above the selected OBBs. Then, the frontal and lateral cameras were adjusted so that the OBBs were in focus and centered in the frame. The measurements were then performed, during which the frontal camera recorded the compression force by tracking the position of the upper plate and the shape of the spheroid. Data processing was carried out in MATLAB using a previously developed model describing compression of an elastic sphere between two planes.[20,21]

$$F = \frac{4}{3} f(\delta) \frac{E}{1-\nu^2} \delta^{\frac{3}{2}} \sqrt{R} \quad (1)$$

where F is the measured compressive force, E is the effective Young's modulus of the spheroid, R is the radius of the spheroid, δ is the deformation of the spheroid, ν is the Poisson's ratio (assumed to be 0.5), and $f(\delta)$ is a multiplicative correction function based on the finite element analysis to account for the large deformations. Although the viscoelastic analysis was not performed in this study, the identical testing parameters were applied to all spheroid types to ensure a valid comparative analysis of the effective Young's modulus

2.11. Preparation of polyethylene glycol-modified fibrin hydrogel

To analyze sprouting, OBBs were encapsulated in a polyethylene glycol (PEG)-modified fibrin hydrogel according to the established protocol.[28] Briefly, a fibrinogen solution derived from the human blood plasma (Sigma-Aldrich, Germany) at a concentration of 25 mg/mL in PBS was prepared; then O,O'-bis2-(N-succinimidylsulfonyloxy)ethyl polyethylene glycol (PEG-NHS) (Sigma-Aldrich, Germany) was added at a molar ratio of 5:1 (PEG-NHS:fibrinogen). The mixture was incubated for 2 h at 37 °C to modify fibrinogen with PEG. Three-day OBBs were extracted from agarose plates and resuspended in the PEG-modified fibrinogen solution. The suspension was then distributed into wells of a 48-well plate (75 μL per well). A thrombin solution from the human blood plasma (0.2 IU/mL; Sigma-Aldrich, Germany) in PBS was prepared separately. An equal volume (75 μL) of the thrombin solution was added to each well containing fibrinogen with OBBs, and the mixture was gently mixed by pipetting to avoid bubble formation. Within 1 min after adding thrombin to fibrinogen, hydrogel polymerization and solidification occurred. The final concentrations of the hydrogel components were 12.5 mg/mL for fibrinogen and 0.1 IU/mL for thrombin. Subsequently, 300 μL of complete medium was added to each well containing the hydrogel-encapsulated OBBs. Encapsulated OBBs were visualized using an EVOS imaging system (Invitrogen, USA), and images were obtained for subsequent analysis. The image analysis included counting sprouts, measuring average sprout length, and calculating sprout area using the Fiji software with the Sprout Morphology plugin.

2.12. Fluorescence lifetime imaging analysis

Fluorescence lifetime imaging microscopy (FLIM) was performed using a two-photon microscopy system (Nikon Ti2-U, Japan) equipped with a time-correlated single-photon counting (TCSPC) FLIM module. Excitation was achieved using a femtosecond pulsed laser (Femto Fiber Ultra 780/920 nm, Toptica, Germany) at 780 nm. Fluorescence detection was performed with a hybrid GaAsP detector (HPM-100-40, Becker & Hickl, Germany) covering the spectral range of 300–720 nm. A BP445/45 bandpass and an SP680 short-pass filter were employed to isolate nicotinamide adenine dinucleotide (NADH) fluorescence. The average excitation power at the sample ranged from 5 to 10 mW, yielding a photon count rate of approximately $1–2 \times 10^5$ photons/s.

The fluorescence decay parameters obtained via multiphoton-FLIM were processed using the SPCImage 9.0 software (Becker & Hickl, Germany). First, FLIM-stacks were spatially binned in an 11 × 11 window, and fluorescence decays $F(t)$ were then fitted with the two-component bi-exponential model:

$$F(t) \sim IRF(t) \otimes (a_1 exp(-\frac{t}{\tau_1}) + a_2 exp(-\frac{t}{\tau_2})) \quad (2)$$

where a_i, τ_i (i = 1,2) are the amplitudes and lifetimes of the i-th component, respectively, and *IRF (t)* is the instrument response function, modeled by a Gaussian function. In addition to these parameters, the mean fluorescence lifetime weighted by the respective component intensity τ_m was estimated as the integral FLIM characteristic:

$$\tau_m = \frac{a_1\tau_1 + a_2\tau_2}{a_1 + a_2} \quad (3)$$

The further processing, including statistical evaluation and visualization, was carried out using Python 3.9 with the NumPy, Pandas, and Matplotlib packages.

2.13. Statistical analysis

Statistical analyses were performed using the GraphPad Prism 8.0 software (GraphPad Software, USA). Data are presented as mean ± standard deviation (SD). For comparisons between two groups, an unpaired Student's *t*-test was used. For comparisons between three or more groups, a one-way analysis of variance (ANOVA) was performed, followed by Tukey's post hoc test for multiple comparisons. The differences were considered statistically significant at $p < 0.05$.

3. Results

3.1. Characterization of stromal cells isolated from oral tissues

The stromal cells isolated from human gingiva and dental pulp consisted of actively proliferating, homogeneous populations that formed confluent monolayers within 2–3 days after passaging. Cells from both cultures exhibited a fibroblast-like morphology typical of stromal cells, characterized by a spindle shape and planar cell polarity (Figure 1A). At the same time, we observed morphological differences between cells from the two tissue sources: stromal cells from the gingiva appeared elongated, whereas pulp-derived cells exhibited a more rounded shape. Cell sizes differed between the two cultures, with pulp-derived cells being significantly larger than gingival cells.

Subsequently, the isolated stromal cells were characterized via ICC staining for key cytoskeletal proteins (Figure 1B), including vimentin (an intermediate filament protein) and fibrillar actin (F-actin). The analysis revealed that, in both cell cultures, actin filaments formed well-developed stress fibers, while vimentin filaments were distributed throughout the cytoplasm, contributing to the maintenance of cell shape. Notably, pulp-derived cells exhibited more extensive spreading on the substrate compared to gingival cells, indicating a higher degree of focal contact formation with the extracellular matrix (ECM). ICC staining for ECM proteins (Figure 1C) demonstrated the deposition of fibronectin and type I collagen in both cultures. Fibronectin appeared as a network of extracellular fibrils, whereas collagen was mainly distributed diffusely within the cells, with a small number of collagen filaments visible in the intercellular space.

Furthermore, we profiled the surface marker expression in cells at passage 5 using flow cytometry (Table 1; Figures S1 and S2). It is important to note that the classical panel of positive MSC markers includes CD105, CD90, and CD73, while negative markers characteristic of hematopoietic and endothelial cells are represented by CD45, CD34, CD14 or CD11b, CD79α or CD19, and HLA-DR.[29] To meet the minimal definition for MSCs, a population must exhibit the expression of positive markers in >95% of cells, while the expression of each negative marker should not exceed 2%. In this study, we expanded the positive marker panel to also include CD44 and CD29,[30] and added CD31 to the negative panel due to its association with platelets, lymphocytes, and endothelial cells.[31]

Based on immunophenotyping results, we confirmed the mesenchymal nature of the isolated cells and the absence of hematopoietic and endothelial cells in the cultures. However, the expression profiles of certain markers, particularly CD90 and CD105, did not meet the criteria for classifying these cells as MSCs, as the proportion of marker-positive cells was below 95%. Accordingly, these cells will be referred to as gingiva-derived and pulp-derived stromal cells, without assigning them to MSCs.

3.2. Characterization of organ building blocks

Gingiva- and pulp-derived stromal cells were used to produce five groups of oral tissue OBBs. The two control groups included OBBs derived from the single cell type — either gingiva-derived cells (G group) or pulp-derived cells (P group). The remaining three groups were fabricated from both cell types using different methods: by mixing gingiva- and pulp-derived cells (M group), by layering gingiva-derived cells on a preformed core, composed of pulp-derived cells (PG group), and, conversely, by layering pulp cells on a core made from gingiva cells (GP group). All OBBs contained 2,000 cells each.

Figure 2 illustrates the dynamics of OBB formation. It can be seen that, on day 0 of culturing (the day of cell seeding onto non-adhesive agarose plates), the diameter of G OBBs was 30 μm larger than that of P OBBs. This observation is interesting because, as previously shown in morphological studies of 2D cultures (refer to section 3.1), pulp cells were

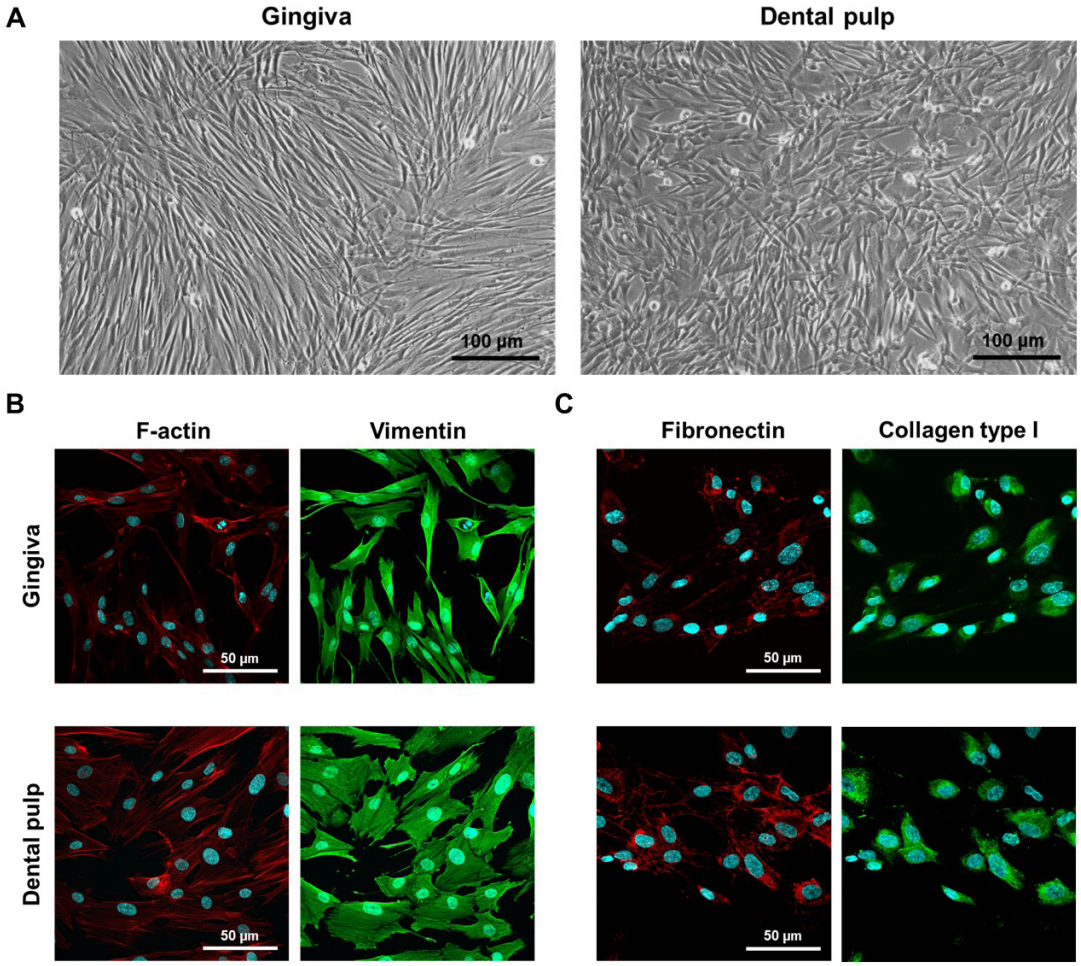

Figure 1. Morphology of stromal cells obtained from the gingiva and dental pulp in 2D cultures. (A) Gingiva and dental pulp-derived cells in a 2D culture. Scale bars: 100 µm; magnifications: 10×. Expression of (B) cytoskeletal (F-actin, red; vimentin, green) and (C) extracellular matrix (fibronectin, red; collagen type I, green) marker proteins in the stromal cells. Scanning confocal microscopy. Nuclei (blue) are stained with Hoechst 33258. Scale bars: 50 µm; magnifications: 40×.

Table 1. Expression of surface markers in gingiva- and pulp-derived stromal cells at passage 5

State	Markers	Gingiva (%)	Dental pulp (%)
Positive	CD44	99.69 ± 0.52	99.9 ± 0.01
	CD90	99.73 ± 0.16	58.85 ± 15.34
	CD105	89.02 ± 9.59	95.21 ± 4.09
	CD73	99.88 ± 0.11	99.96 ± 0.05
	CD29	99.46 ± 0.87	99.84 ± 0.25
Negative	CD31	0.09 ± 0.09	0.09 ± 0.10
	CD19	0.66 ± 0.20	0.32 ± 0.13
	CD11b	0.06 ± 0.05	0.17 ± 0.17
	CD45	0.71 ± 0.65	0.65 ± 0.58
	CD34	0.25 ± 0.28	0.38 ± 0.46
	HLA-DR	2.21 ± 1.71	1.17 ± 0.76

Abbreviations: CD: Cluster of differentiation; HLA-DR: Human leukocyte antigen–D-related.

larger than gingiva cells. Therefore, the corresponding OBBs were expected to reflect this size relationship. By day 9 of the experiment, G OBBs became more than 50 μm larger than those from the P group, with the diameters of 196 ± 7.3 μm and 150 ± 6.5 μm, respectively. Overall, G OBBs decreased in size by approximately 150 μm from their initial diameters, while P OBBs decreased by about 180 μm. It can also be noted that the compactization of P OBBs occurred gradually, whereas G OBBs demonstrated a sharp decrease in the diameter (~ 100 μm) within the first day of culturing.

Analyzing the formation dynamics of OBBs derived from the two cell types revealed the following trends (Figure 2). On day 0 of the experiment, the diameter of M OBBs was 308 ± 4.9 μm, which was comparable to the size

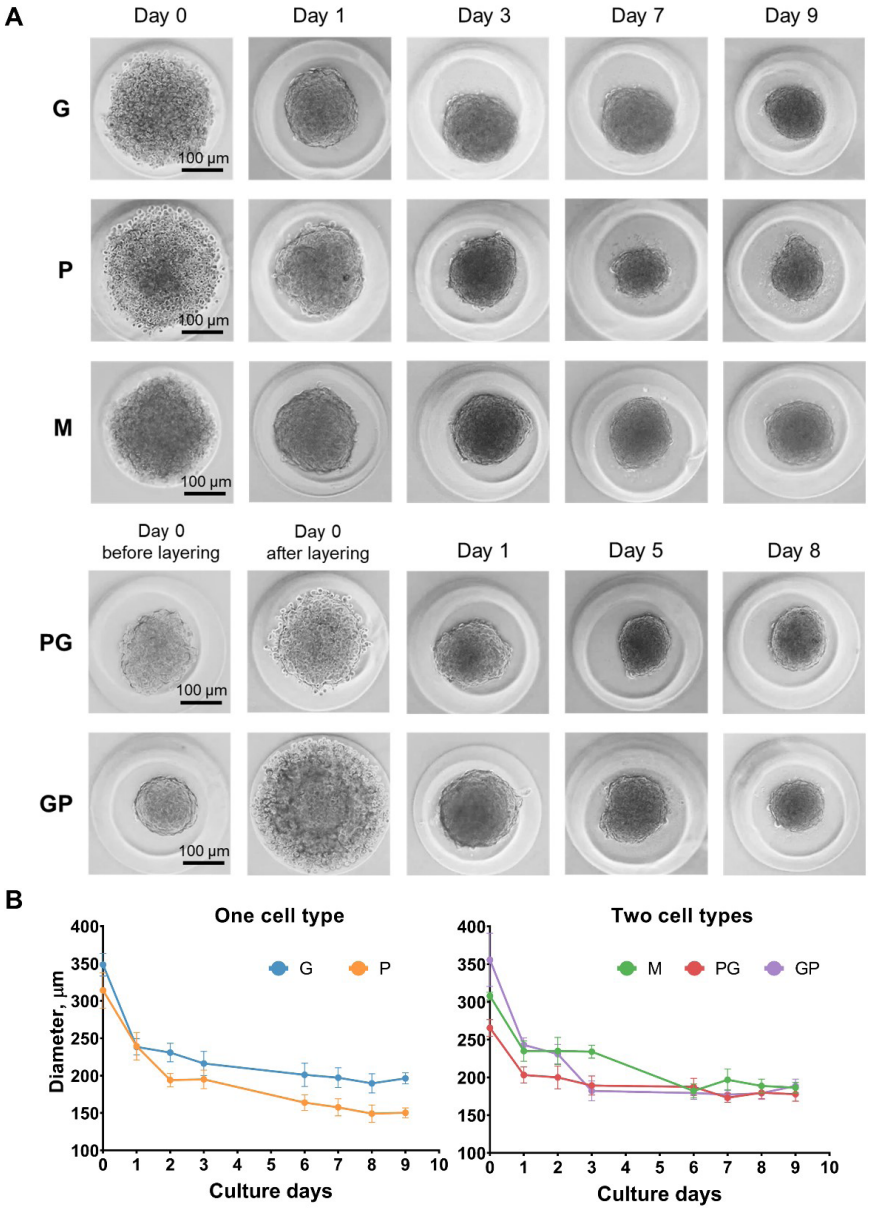

Figure 2. Formation and compactization of oral tissue organ building blocks (OBBs). (A) Representative micrographs. Scale bars: 100 μm; magnifications: 10×. (B) Formation dynamics. Ten OBBs were analyzed for each experimental point. Data on graphs are presented as mean ± SD.
Notes: G: Gingiva-derived cells; GP: Layering pulp-derived cells on a core composed of gingiva-derived cells; M: Mixing gingiva- and pulp-derived cells; P: Pulp-derived cells; PG: Layering gingiva-derived cells on a core composed of pulp-derived cells.

of P OBBs (314 ± 14.8 μm). However, by day 9, the size of M OBBs (187 ± 7.2 μm) was almost equal to that of G OBBs (196 ± 7.3 μm). The diameter of PG OBBs was the smallest among all the experimental groups on day 0, averaging 265 ± 11.1 μm. However, by the end of the observation period, the size of these OBBs was intermediate between that of P OBBs (150 ± 6.5 μm) and G OBBs (196 ± 7.3 μm), with a diameter of 177 ± 9.2 μm. The diameter of GP OBBs was comparable to that of G OBBs both at the beginning and at the end of the culturing period: their size was 355 ± 30.7 μm on day 0 and 189 ± 8.9 μm on the final day. Their formation dynamics were also similar to that of G OBBs, with a noticeable decrease in the diameter of about 100 μm occurring within the first 24 h of culturing.

3.3. Morphological analysis of organ building blocks

The cells in G OBBs were oval or round, with basophilic nuclei (Figure 3A). The intercellular spaces were slightly expanded, potentially indicating differences in the cellular adhesive properties compared to those of the dental pulp. The general shape of the OBBs remained symmetrical and well-formed. The OBBs were spherical and ellipsoidal when visualized by MUSE. They were composed of large, loosely arranged cells with well-defined eosinophilic cytoplasm. The structure of OBBs was uniform, with weakly contrasting Hoechst-stained nuclei standing out against the background of the pink eosinophilic mass. The average distance between the nuclei was 8 μm (Figure 3F).

P OBBs had a dense, compact structure with a uniform distribution of cellular elements (Figure 3B). The cells were large, with clearly visible basophilic nuclei. The intercellular spaces were almost absent, indicating a high degree of cellular adhesion. Areas of necrosis or ruptures of the structure were not observed. When examined by MUSE, the samples had a spherical shape with a relatively smooth surface and were composed of cells with large nuclei and poorly developed cytoplasm. A bright blue glow of the Hoechst solution staining DNA and the almost complete visual absence of an eosinophilic cytoplasm were noted. The structure of the OBBs was uniform. The distance between the nuclei was ~5.5 μm (Figure 3G).

M OBBs derived from equal proportions of pulp- and gingiva-derived stromal cells demonstrated a mixed morphotype and variability in the density of cell packing (Figure 3C). The interaction between these two cell types led to the formation of heterogeneous areas. In some OBBs, areas of compactization were observed (indicating pulp-derived cells), while in others, a looser structure (gingiva-derived cells) was observed. Such changes may be associated with the differences in the adhesive properties and metabolic activity of cells. When observed using MUSE, the samples were small, spherical or hemispherical, with an uneven surface, pronounced fluorescent nuclei, and narrow layers of eosinophilic cytoplasm. The distance between the nuclei was ~6.5 μm (Figure 3H).

The reverse arrangement of cells in PG OBBs led to the inversion of the morphological features of the OBBs (Figure 3D). The inner part, represented by the pulp cells, was characterized by dense packing and intensely stained nuclei. The outer part, on the contrary, was looser, creating

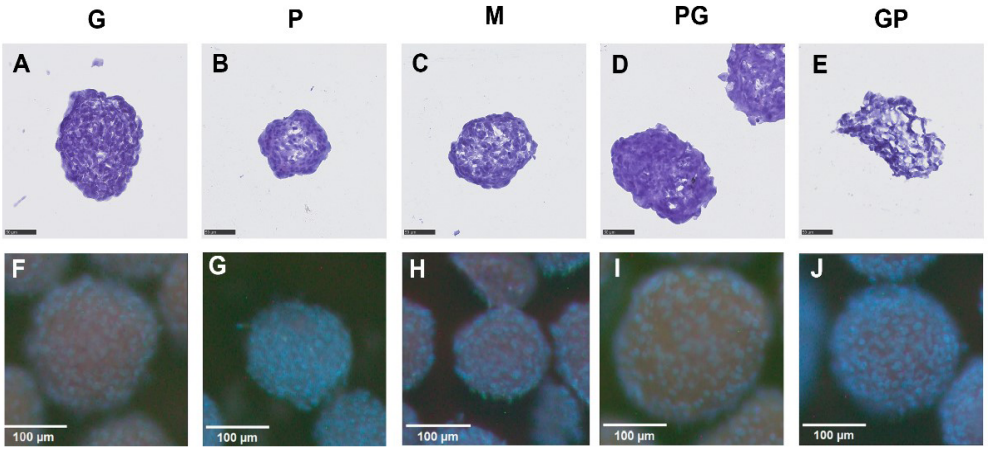

Figure 3. Histological analysis of organ building blocks (OBBs). The OBBs from (A & F) G, (B & G) P, (C & H) M, (D & I) PG, and (E & J) GP, stained with (A–E) hematoxylin and eosin or (F–J) Hoechst 33258 and eosin, visualized using (A–E) light microscopy (scale bars: 50 μm; magnifications: 40×) and (F–J) microscopy with ultraviolet excitation (scale bars: 100 μm; magnifications: 10×).
Notes: G: Gingiva-derived cells; GP: Layering pulp-derived cells on a core composed of gingiva-derived cells; M: Mixing gingiva- and pulp-derived cells; P: Pulp-derived cells; PG: Layering gingiva-derived cells on a core composed of pulp-derived cells.

a characteristic density gradient from the center to the periphery. When examined by MUSE, the samples were large, spherical or hemispherical, with a large amount of eosinophilic cytoplasm and loosely arranged, low-contrast nuclei. The surface was smooth. The distance between the nuclei was ~15 μm (Figure 3I).

The structure of GP OBBs demonstrated clear separation between the inner gingival cells and the outer pulp cells (Figure 3E). The inner part of the OBBs (gingiva-derived cells) appeared loose, with large intercellular spaces, while the outer part (pulp-derived cells) was observed as a dense pack of cells. This organization may be due to the directed adhesion of pulp-derived cells to the outer surface of the OBBs, while the gingival cells remained less densely packed within. When examined by MUSE, the OBBs were spherical and ellipsoidal, with an uneven surface and a pronounced fine-grained structure formed by the nuclei of pulp cells located on the surface. Brightly fluorescent blue nuclei contrasted with the eosinophilic cytoplasm of the gingival cells, forming the internal core of the OBBs. The distance between the nuclei was ~6 μm (Figure 3J).

3.4. Spreading test

All experimental OBB groups adhered to the adhesive plastic within 1–2 h after seeding and subsequently began spreading (Figure 4A). Almost all groups showed a surge in the spreading rates after day 4 of culturing. By day 6, the spreading areas increased fourfold in the M and GP groups, and nearly 3.5 times in the G and PG groups, compared to their corresponding areas on day 4. Moreover, on day 6, all OBB groups fully transitioned into monolayers, except for the P group, where the initial cell aggregates persisted. In some cases, the complete transition to a cell monolayer for this group took 7–9 days (Figure 4B). We also noticed that the spreading rate of P OBBs was the lowest among all groups; nonetheless, by day 6, their spreading area had increased approximately twofold compared to that on day 3. The GP and PG groups demonstrated the most active spreading among all groups. By day 3, PG and GP OBBs had disassembled to more than halfway, and by day 5, they had almost completely transitioned into monolayers (Figure 4A). The M group exhibited a similar trend, but at a slightly slower pace than the other two mixed-cell groups.

3.5. Biomechanical properties of organ building blocks

Next, we studied the bulk mechanical properties of the 3-day OBBs using parallel-plate compression testing. The Young's modulus, which characterizes the stiffness, was calculated for each tested sample. Figures 5 and S3 and Table S1 summarize the results of the experiment. The P OBBs exhibited the highest stiffness, with an average Young's modulus of 1.6 ± 0.6 kPa (Figure 5A). In contrast, the G OBBs showed a Young's modulus value of 0.8 ± 0.5 kPa, the lowest among all groups. Differences in Young's moduli between OBBs derived from the two cell types (M, GP, and PG) were not statistically significant; their stiffness values were approximately 1 kPa.

The experiment with 7-day OBBs revealed similar trends (Figure 5B). P OBBs proved to be the stiffest, with an average Young's modulus of 3.7 ± 1.7 kPa, which was 2.1 kPa higher than that of the 3-day OBBs. In addition, G OBBs were the softest, with an average Young's modulus of 0.8 ± 0.4 kPa. Interestingly, we did not observe any differences in the Young's modulus between the 3-day and 7-day G OBBs (Figure 5C). Furthermore, there were no significant differences in Young's moduli among the M, GP, and PG groups. However, we observed that in the M and PG groups, there was a statistically significant increase in the average Young's modulus compared to that of the 3-day OBBs.

3.6. Marker protein expression in organ building blocks

All OBB groups were stained for cytoskeleton (vimentin and F-actin) and ECM proteins (fibronectin and collagen type I). Figure 6 shows that vimentin and F-actin were well visualized within cells of OBBs across all groups. Vimentin (Figure 6A) was expressed throughout the entire volume of OBBs. Staining for F-actin showed that this protein was distributed chaotically within cells, forming stress fibers. No significant differences in the cell distribution were observed between OBBs from the five groups. Finally, staining for structural proteins helped visualize the OBBs' shape. Notably, in the P group, OBBs were spherical with a smooth, uniform surface and highly compacted, unlike the other OBB groups.

Collagen type I was detected in all OBB groups. It was predominantly localized in the center of each OBB across all groups, forming a dense ECM core (Figure 6B). In the M group, the collagen cores were most distinctly visible. Fibronectin was evenly distributed throughout the OBBs, forming a clearly distinguishable network of filaments.

3.7. Sprouting of organ building blocks within a fibrin hydrogel

Here, we studied the sprouting of OBBs by encapsulating them in a PEGylated fibrin hydrogel and culturing them for 10 days. During the experiment, analyses were conducted on days 3, 7, and 10, assessing parameters such as the number of sprouts per OBB, the average sprout length, the total sprout area per OBB, and the average number of junctions (branching points) per OBB. We found that

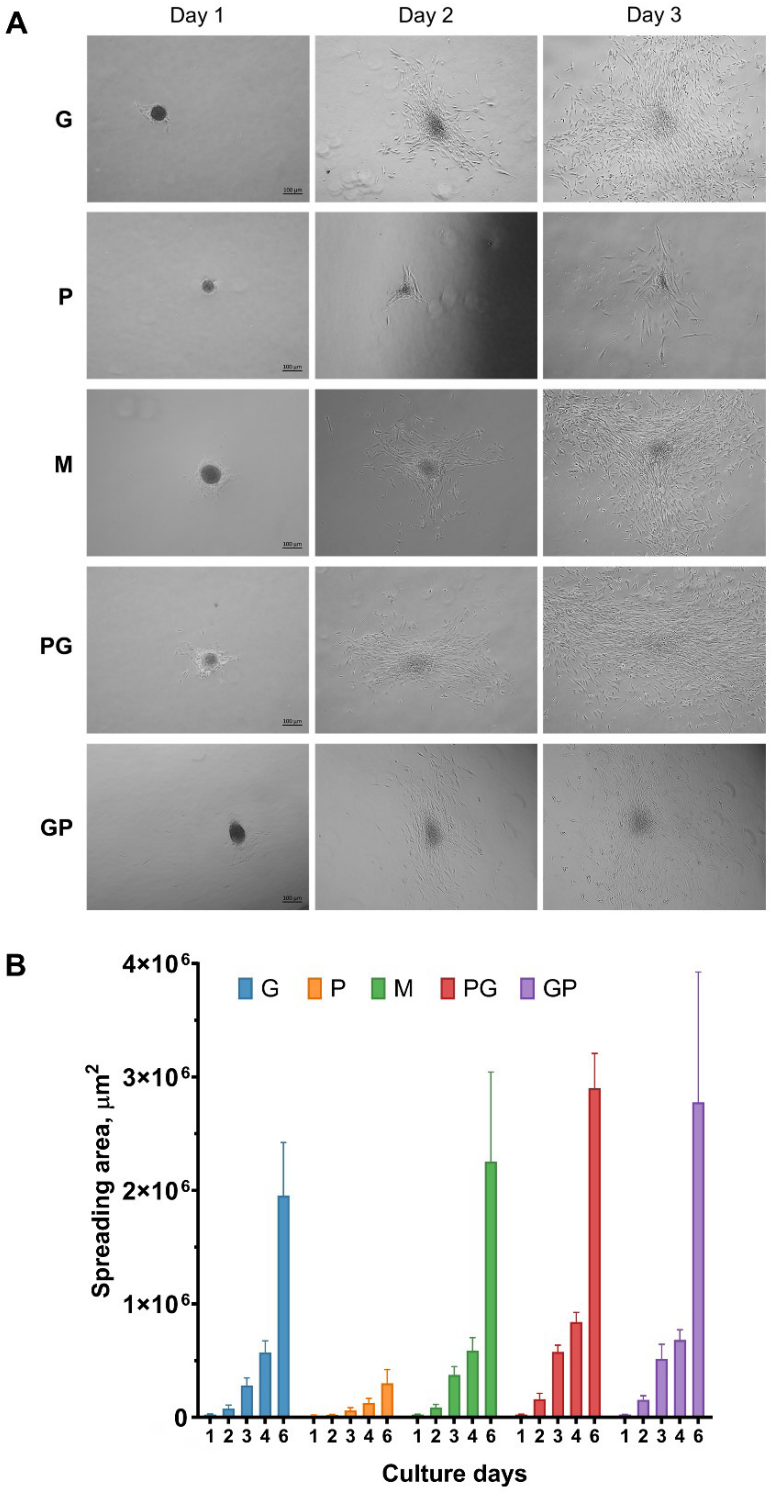

Figure 4. Spreading of oral tissue organ building blocks (OBBs). (A) Morphology of spreading. Scale bars: 100 μm; magnifications: 5×. (B) Spreading rates. The spreading area also includes the contact area between the OBBs and the surface. Ten OBBs were analyzed for each experimental point. Data on graphs are presented as mean ± SD.

Notes: G: Gingiva-derived cells; GP: Layering pulp-derived cells on a core composed of gingiva-derived cells; M: Mixing gingiva- and pulp-derived cells; P: Pulp-derived cells; PG: Layering gingiva-derived cells on a core composed of pulp-derived cells.

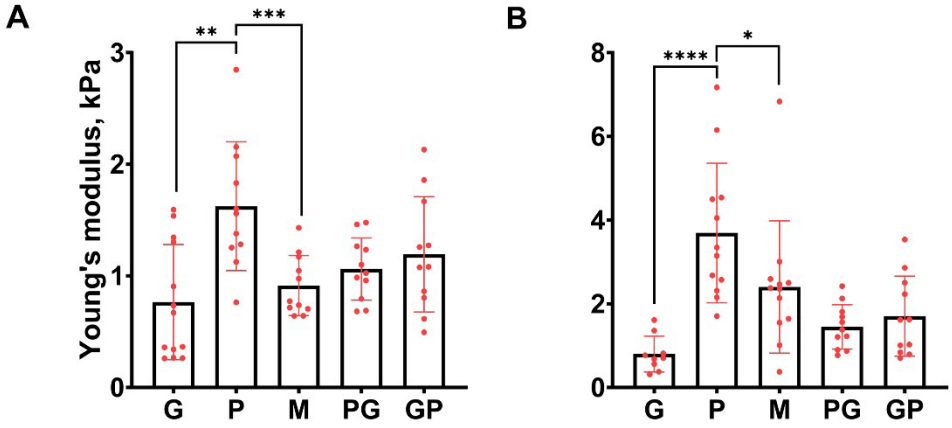

Figure 5. Biomechanical properties of the oral tissue organ building blocks (OBBs). Average Young's moduli of (A) 3-day and (B) 7-day OBBs.
Notes: Data on graphs are presented as mean ± SD. $^{**}p < 0.01$, $^{***}p < 0.001$, $^{****}p < 0.0001$. G: Gingiva-derived cells; GP: Layering pulp-derived cells on a core composed of gingiva-derived cells; M: Mixing gingiva- and pulp-derived cells; P: Pulp-derived cells; PG: Layering gingiva-derived cells on a core composed of pulp-derived cells.

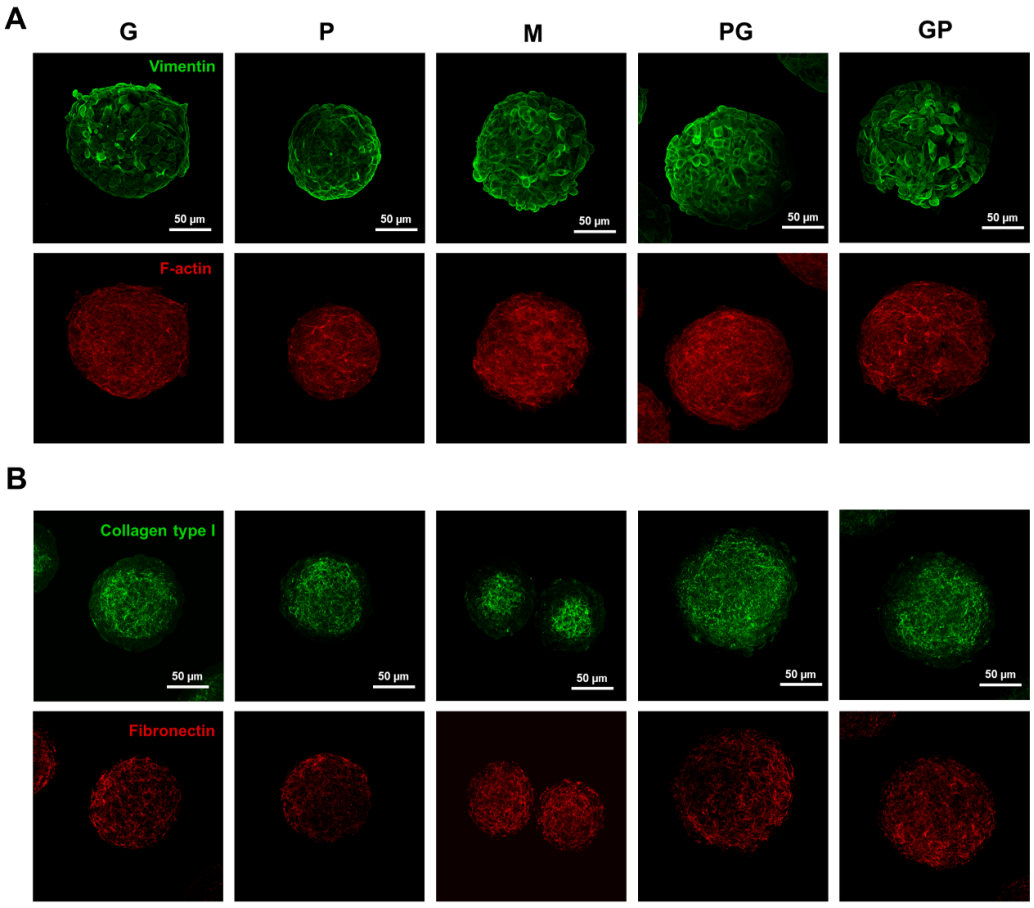

Figure 6. Expression of marker proteins in organ building blocks (OBBs). (A) Distribution of cytoskeleton proteins: vimentin (green) and F-actin (red). (B) Localization of extracellular matrix proteins: collagen type I (green) and fibronectin (red). Scanning confocal microscopy. Scale bars: 50 μm; magnifications: 40×.
Notes: G: Gingiva-derived cells; GP: Layering pulp-derived cells on a core composed of gingiva-derived cells; M: Mixing gingiva- and pulp-derived cells; P: Pulp-derived cells; PG: Layering gingiva-derived cells on a core composed of pulp-derived cells.

all OBB types formed sprouts within the fibrin hydrogel starting from day 3 after the encapsulation. Figure 7A shows that, in all groups, except for the G group, there was a significant increase in the number of sprouts over time. Notably, the P group exhibited a more gradual increase, unlike the M, PG, and GP groups, where there was a surge in the number of sprouts when shifting from day 3 to day 7. At day 10, the number of sprouts per OBB averaged between 10 and 12 units in the groups P, M, PG, and GP, with no statistically significant differences observed

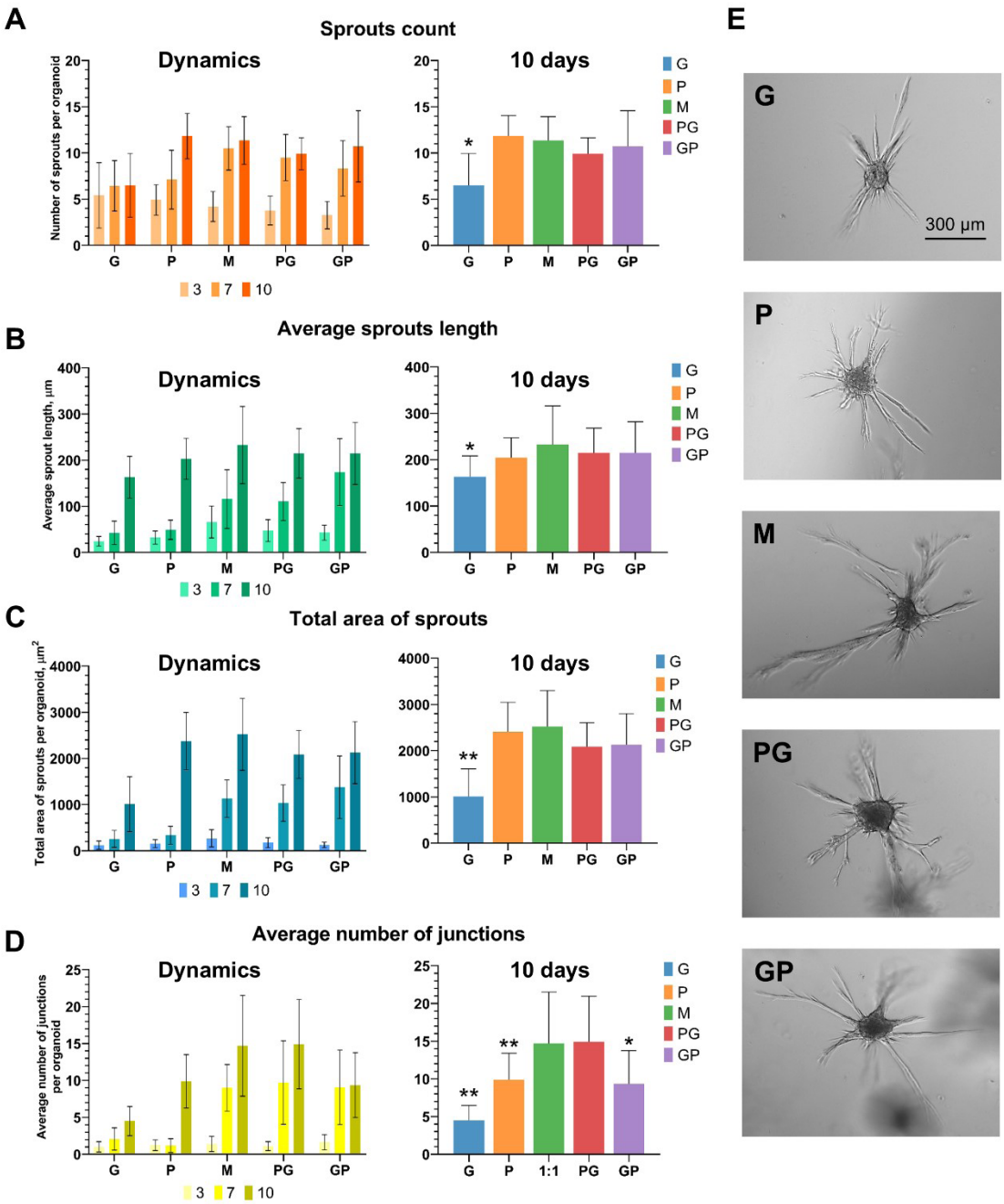

Figure 7. Sprouting of organ building blocks (OBBs) within fibrin hydrogel. (A) Average number of sprouts per OBB, (B) average sprout length, (C) total area of sprouts per OBB, and (D) average number of junctions per OBB across culturing (left diagrams) and at day 10 of culturing (right diagrams). Data on graphs are presented as mean ± SD. (E) Morphology of sprouted OBBs at day 10. Scale bar: 300 μm; magnifications: 10×.
Notes: *$p < 0.05$, **$p < 0.01$; G: Gingiva-derived cells; GP: Layering pulp-derived cells on a core composed of gingiva-derived cells; M: Mixing gingiva- and pulp-derived cells; P: Pulp-derived cells; PG: Layering gingiva-derived cells on a core composed of pulp-derived cells.

between these groups. The G group had a significantly lower number of sprouts (approximately 7 units per OBB) compared to other groups.

Furthermore, we demonstrated that in all OBB groups, sprouts significantly grew by day 10 (Figure 7B). The increase in the sprout length in the G and P groups occurred sharply after day 7, whereas in the OBB groups with two cell types, sprouting was more gradual. The average sprout length did not differ significantly among the groups P, M, PG, and GP, ranging from 200 to 230 μm. In contrast, the G group showed a significantly lower length (160 μm) compared to other groups.

The total area of sprouts per OBB (Figure 7C) increased by 3–5 times by day 7 in the M, PG, and GP groups compared to day 3, while, in the G and P groups, there was almost no change between days 3 and 7. Notably, the G group lagged significantly behind the others. In groups P, M, PG, and GP, the mean area values ranged from 2,000 to 2,500 μm^2, with differences between these groups being insignificant; in contrast, the area in the G group was close to 1,000 μm^2.

The number of junctions (branching points) correlated with the increase in the total sprout area across all OBB groups (Figure 7D), showing little difference between the groups M and PG, both averaging around 15 units. The lowest averaged junction number (4.5 units) was observed in the G group, whereas in the P and GP groups, it reached 9.5–9.8 units, with no significant difference between these two groups. Figure 7E shows the morphology of sprouted OBBs within the fibrin hydrogel at day 10.

3.8. Fluorescence lifetime imaging microscopy parameters for stromal cell organ building blocks of different types

The mean fluorescence lifetime τ_m maps indicate that the fluorescence properties of the dental pulp and gingiva-derived stromal cells differed from each other (Figure 8A). As such, the most noticeable differences were evident from observing the layered OBBs with the pulp cells in the center: there was approximately a two times difference in the fluorescence emission intensity between the inner layers and the outer layers, indicating that the pulp stromal cells exhibit intense fluorescence emission with two-photon excitation at 780 nm in comparison to the gingiva-derived stromal cells. The τ_m ranges also differed: τ_m of the pulp cells was 550–750 ps, while those of the gingiva stromal cells were 700–900 ps.

This evidence is further supported by the representative maps for single-cell type culture OBBs. The distribution of the FLIM decay parameters a_1, τ_2, and τ_m for each group is shown in Figure 8B–D. The distribution for τ_m proves the observation that the G group exhibited a longer τ_m, with a median value of 783 ps (interquartile range [IQR]: 733–842 ps), whereas that for the P group was 716 ps (IQR: 682–750 ps) (Figure 8B). Furthermore, the distributions for the relative intensity of the short-lifetime component a_1 showed that the aforementioned difference in τ_m does not come from different intensity proportions between the two components, as the median values for both the P

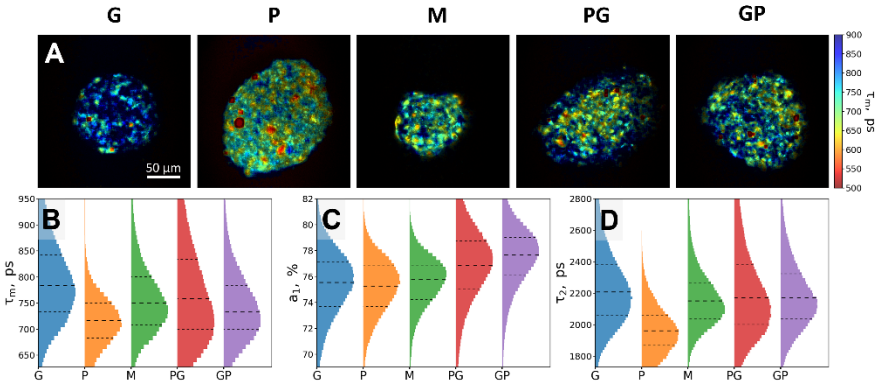

Figure 8. Fluorescence lifetime imaging microscopy (FLIM) parameters for stromal cell organ building blocks (OBBs). (A) Representative color-coded maps of mean fluorescence lifetime τ_m weighted by the normalized pixelwise photon counts for a two-component bi-exponential decay curve fit of FLIM parameters across groups: G, P, M, PG, and GP. Scale bars: 50 μm; magnifications: 40×. Histograms of per-pixel FLIM parameter distributions compared across groups: (B) mean fluorescence lifetime weighted with component intensities τ_m, (C) relative intensity of the first, short-lifetime fluorescence emission component a_1, and (D) fluorescence lifetime of the second, long-lifetime emission component τ_2. Thick and thin dashed lines correspond to distribution medians and interquartile ranges, respectively.

Notes: G: Gingiva-derived cells; GP: Layering pulp-derived cells on a core composed of gingiva-derived cells; M: Mixing gingiva- and pulp-derived cells; P: Pulp-derived cells; PG: Layering gingiva-derived cells on a core composed of pulp-derived cells.

and G groups were close to 75% (Figure 8C). Instead, one can observe the difference in the estimated fluorescence lifetime of the longer-living component τ_2, with the median values of the P and G groups being 1,962 ps (IQR: 1,868–2,058 ps) and 2,210 ps (IQR: 2,058–2,380 ps), respectively (Figure 8D).

4. Discussion

The use of 3D cell cultures as a component of bioinks is becoming increasingly widespread. Processes of cells' self-organization, such as migration, differentiation, synthesis of signaling factors, and ECM formation within spheroids and OBBs, enable the controlled and efficient maturation of the printed construct during the post-printing stage [32]. Here, for the formation of OBBs for periodontal regeneration, we used cells localized within the oral tissues based on their properties and biological roles. Gingiva- and pulp-derived stromal cells within OBBs perform specific functions crucial for the stability and maturation of the resulting periodontal bioequivalents. Additionally, these two cell types can influence each other *in vitro*, enhancing certain mutual capabilities.

Dental pulp-derived cells are known for their high potential for osteogenic differentiation.[22,33] Several studies have shown that decellularized ECM of pulp-derived cells promotes the osteogenic differentiation of gingiva-derived stromal cells.[34,35] It is also known that the ECM of pulp-derived cells contains proteins such as tenascin and osteonectin, which are almost absent in the ECM of gingiva-derived cells.[36] Therefore, pulp-derived cells serve as a potential source of osteoblasts and mineralized matrix in printed periodontal constructs.

Gingiva-derived stromal cells, as a primary cell type within the periodontal complex, coordinate wound healing processes in response to injuries.[34] They exhibit a more pronounced migratory activity compared to that of pulp-derived cells, as was shown in a scratch assay;[37] the ECM of dental pulp-derived cells can stimulate this activity. Thus, gingival cells can be considered a dynamic component of the bioequivalent, contributing to tissue integrity. Finally, gingival and dental pulp tissues are well-known sources of stromal cells due to their accessibility: both tissues can be easily obtained during routine wisdom tooth extraction procedures.[38]

Spheroids from gingiva- and pulp-derived stromal cells have been described in the literature, and many of their properties have been characterized. For example, it is known that spheroids from gingiva-derived stromal cells decrease in size over time during culturing, regardless of their initial size.[39-41] They are positively stained for CD73, vimentin, fibronectin,[40] collagen type 1 alpha 2 (COL1A2), platelet-derived growth factor receptor beta (PDGFRβ), integrin beta-1 (Itgβ1), and alpha-smooth muscle actin (αSMA).[41] Additionally, they maintain cell viability for at least seven days of culturing.[39] Spheroids formed from dental pulp-derived stromal cells have also been characterized in considerable detail. In particular, studies have investigated the dynamics of spheroid formation depending on the initial cell density.[42,43] Furthermore, several studies have demonstrated the enhanced capacity of pulp cells cultured in spheroids to differentiate in the osteogenic lineage.[43,44] In the current study, for the first time, we produced complex stromal spheroidal OBBs that included both gingiva- and pulp-derived cells. We generated three groups of such OBBs with different designs to determine whether the mutual arrangement of cells within an OBB affects the properties of a 3D cell structure. Subsequently, we analyzed the OBBs using various methods. We started with examining changes in diameter over time.

Spherical 3D cell cultures, such as spheroids and organoids, are known to change their size during culturing. The main factors influencing the size of a cell aggregate include the cell type and the culturing conditions. Changes in diameter over time can serve as an indirect indicator to assess the structural organization of a spheroid or organoid and study cell interactions within it. Some types of organoids, such as cerebral organoids[45,46] or cartilage microtissues,[47] are capable of growing over time, increasing in size, and acquiring a more complex structure. Spheroids derived from tumor cells typically increase significantly in size over time because malignant cells do not exhibit contact inhibition.[48] Conversely, most 3D cultures obtained from stromal cells show cessation of cell proliferation and a marked decrease in size during culturing. This is associated with compactization—a process by which a spheroid or an organoid acquires a denser structure due to the increased cell–cell and cell–ECM contacts.[49-51] Consequently, analyzing the dynamics of compactization was the first step in characterizing the oral tissue OBBs. We found that all groups significantly decreased in size by day 9 of culturing. The most important stage of compactization occurred at day 0, when the loose cell aggregate acquired a compact spherical shape. In some OBB groups, the diameter decreased to 100 μm at this stage (Figure 2).

Spreading is the ability of spherical 3D cell cultures to form a monolayer of cells when placed in adhesive conditions.[52,53] Studying OBBs' spreading can be important from the perspective of their use as structural units in 3D bioprinting, since this feature allows understanding how quickly and effectively cells can migrate from cell

aggregates and colonize the printed construct. In this experiment, we found that OBBs composed of two cell types (M, GP, and PG) spread more fully and actively than the G and P OBBs (Figure 4). Such a result may indicate that gingiva- and pulp-derived stromal cells within the two-cell type OBBs maintain a more physiological state than that in monocultures. This could be facilitated by secreted proteins and extracellular vesicles, intercellular contacts, and biomechanical stimuli. The higher spreading rates also suggest that OBBs composed of two cell types would colonize the hydrogel scaffold more quickly and efficiently after 3D bioprinting than single cell type OBBs would do.

To study the internal structure of the OBBs, we performed ICC staining of the main cytoskeleton and ECM proteins. Firstly, the fact that all cells within OBBs expressed vimentin and produced ECM proteins indicates that they do not undergo epithelial–mesenchymal transition over time, maintaining their mesenchymal phenotype. The formation of collagen cores suggests that structured, compacted OBBs are formed by day 7 of culturing. The most distinct inner cores were found in M OBBs (Figure 6). However, the mechanisms underlying the development of such internal structures through cell self-organization remain to be elucidated in future studies. Overall, the formation of collagen cores in all the OBB groups results from their compactization and structural separation into a dense outer layer, where cells are tightly in contact with each other, and an inner, looser part where the ECM accumulates.

Studying the mechanical properties of tissues and biomaterials is important for creating biocompatible tissue-engineered constructs capable of performing their functions after transplantation at the injured site. 3D cell cultures, spheroids, organoids, and OBBs can exhibit various levels of stiffness and elasticity depending on the cells they are composed of, as well as on the formation conditions.[53] The OBBs' features may have a critical impact on the resulting properties of the printed bioequivalent. Therefore, it is essential to thoroughly investigate the mechanical properties of OBBs for their subsequent use in 3D bioprinting. Here, we demonstrated that P and G OBBs had different Young's moduli: day 3 P OBBs were approximately twice as stiff as G OBBs, and day 7 P OBBs were 4.6 times stiffer. This may be related both to the biomechanical properties of the cells and to the more active synthesis of ECM proteins by the pulp-derived cells. Additionally, this agrees with a dense cell packing observed in P OBBs (Figure 3). Meanwhile, OBBs composed of the two cell types exhibited intermediate stiffness values that fell between those of the G and P groups. G and GP OBBs did not change their stiffness parameters over four days of culturing, maintaining nearly identical Young's modulus values on days 3 and 7. The rest of the OBB groups increase their stiffness during culturing, potentially due to the accumulation of ECM over time. The measured Young's modulus values of the spheroids fall within the range previously reported for similar spheroid types.[49,53] Although bioprinting was not performed in the present study, spheroids with comparable mechanical properties have been demonstrated to be suitable for extrusion-based bioprinting.[54,55] Therefore, we predicted that OBBs from the G group are probably unsuitable for use as a cellular component of bioinks, as they have a very low stiffness and are likely to be damaged during 3D bioprinting. Meanwhile, OBBs from the M, GP, and PG groups have the Young's moduli that correspond to a combination of the properties of the soft G OBBs and stiff P OBBs, making them more suitable as components of bioinks.

The ability to form sprouts within a hydrogel is an important feature of spheroids and OBBs as cellular components of bioinks and, subsequently, as integral parts of bioequivalents. The degree of this ability indicates how quickly and effectively the hydrogel volume will be filled with cells during the maturation of the printed tissue.[56] All OBB groups, except for the G group, demonstrated a significant dynamic of sprouting, forming 10–15 branched sprouts by day 10 of culturing, with lengths of sprouts comparable to or exceeding the OBBs' diameters (Figure 7). Additionally, in the M, PG, and GP groups, a noticeable increase in the average sprout length, total sprout area, and number of branching points was observed as early as day 7, unlike in the G and P groups. As a result, we suggest that OBBs derived from the two cell types adapt to the hydrogel microenvironment more quickly than OBBs composed of gingiva or pulp monocultures. Future studies will focus on the sprouting processes after 3D bioprinting when OBBs are incorporated into bioinks.

The analysis of the τ_m and FLIM decay parameters revealed distinct metabolic profiles between gingiva- and pulp-derived stromal cells as part of OBBs. Pulp stromal cells exhibited significantly shorter τ_m values (median: 716 ps, IQR: 682–750 ps) compared to those for gingival stromal cells (median: 783 ps, IQR: 733–842 ps), suggesting a higher contribution of glycolytic metabolism in pulp cells.[57] Despite similar proportions of the short-lifetime component ($a_1 \approx 75\%$), the longer fluorescence lifetime component (τ_2) differed markedly between groups, with pulp stromal cells displaying shorter τ_2 values (median: 1,962 ps) relative to gingival stromal cells (median: 2,210 ps). These differences indicate that the shift in τ_m is not due to a change in the ratio of free to protein-bound

NADH, but distinct metabolic profiles linked to their physiological functions: pulp cells, adapted to hypoxic niches, show shorter NADH fluorescence lifetimes (τ_m and τ_2) due to glycolytic dominance and NADH binding to transient complexes such as lactate dehydrogenase, while gingival cells display longer τ_2 from efficient oxidative phosphorylation and stable NADH–enzyme interactions (e.g., complex I). These differences arise from the pulp's role in dentin regeneration (glycolysis-driven biosynthetic demands) versus the gingiva's need for rapid wound healing and immune defense (oxidative phosphorylation-dependent energy). Thus, gingival stromal cells appear to rely more heavily on oxidative phosphorylation, while pulp stromal cells preferentially utilize glycolytic pathways. The twofold higher fluorescence intensity in pulp cells further supports elevated glycolytic activity, consistent with NADH accumulation. These findings align with the established FLIM–metabolism correlations, in which oxidative phosphorylation elongates τ_m and τ_2 via protein-bound NADH in mitochondria.[58] It is important to note that, while FLIM provides a powerful, non-invasive measurement of cellular metabolism, the interpretation of NADH lifetime data can be influenced by factors beyond the free/bound NADH ratio. These include the cell density, microenvironmental conditions, and optical properties of the sample. Although we controlled the measurement conditions, and the observed differences align with the functional adaptation of these cell types, the direct linkage to glycolytic and oxidative phosphorylation rates could be further solidified in future work based on the parallel molecular analysis and functional metabolic assays. Nevertheless, the robust differences in τ_m and τ_2 reported here provide a strong foundation for using FLIM as a rapid, non-damaging assessment of metabolic changes in living systems, including cell organoids.

The metabolic differences between gingiva- and pulp-derived stromal cells revealed by the FLIM analysis have significant implications for bioprinting applications, since these distinct OBBs' energy production pathways directly influence their suitability as bioink components. Pulp stromal cells' glycolytic phenotype suggests better adaptation to hypoxic conditions typical inside thick bioprinted constructs, while gingival cells' oxidative phosphorylation dominance may require rapid vascularization for survival. The twofold higher NADH intensity in pulp cells provides a potential quality control marker for the bioink's homogeneity, and the τ_2 differences indicate varying protein-bound NADH microenvironments that could affect ECM remodeling. These findings enable strategic cell type selection or blending—pulp-derived OBBs for avascular tissue regeneration and gingival cells for vascularized grafts—while the FLIM parameters offer non-destructive metrics for monitoring the metabolic state throughout the bioprinting process, from the bioink preparation to the post-printing maturation. The data underscores the importance of considering native metabolic profiles when developing OBB-based bioinks to ensure the proper function and integration in the engineered tissues.

5. Conclusion

In this study, we generated and characterized OBBs derived from pulp and gingiva cells using various methods. We found that the G and P groups, derived from monocultures of gingiva and pulp cells, respectively, are not optimal for 3D bioprinting due to their specific characteristics: G OBBs exhibit limited mechanical stiffness and the slowest sprouting rates in a hydrogel, while P OBBs demonstrate the poorest spreading ability. Combining the two cell types improved the structural, mechanical, and functional properties of the OBBs. Summarizing our results, we conclude that all three types of two-cell type OBBs can be effectively used as cellular components of bioinks, with different designs suited for specific applications. Where properties of pulp cells are critically important—for example, in creating stiff, thick-layered constructs with a hypoxic microenvironment—GP OBBs are most suitable. Conversely, the dominant features of gingiva cells in PG OBBs will be advantageous for printing soft, vascularized bioequivalents. OBBs of the M group, combining properties of both cell types equally, are optimal for fabricating medium-stiffness constructs with moderate hypoxia.

Acknowledgments

The research was conducted at the scientific base of the laboratory established within the framework of the Academic Leadership Program "Priority 2030."

Funding

The work was carried out with financial support from the Ministry of Science and Higher Education of the Russian Federation under grant number 075-15-2024-640 (Sechenov University).

Conflict of interest

The authors declare they have no competing interests.

Author contributions

Conceptualization: Nastasia V. Kosheleva, Polina Y. Bikmulina

Data curation: Lidiia R. Grinchevskaia, Anna V. Kardosh, Vitalia R. Izhbulatova, Yuri M. Efremov, Artem M. Mozherov, Alexey L. Fayzullin, Polina Y. Bikmulina,

Oleg O. Pavlov, Boris P. Yakimov

Formal analysis: Lidiia R. Grinchevskaia, Anna V. Kardosh, Daria S. Kuznetsova, Oleg O. Pavlov, Boris P. Yakimov

Funding acquisition: Peter S. Timashev

Investigation: Lidiia R. Grinchevskaia, Anna V. Kardosh, Vitalia R. Izhbulatova, Daria S. Kuznetsova, Yuri M. Efremov, Artem M. Mozherov, Alexey L. Fayzullin

Methodology: Daria S. Kuznetsova, Yuri M. Efremov, Artem M. Mozherov, Alexey L. Fayzullin, Polina Y. Bikmulina, Oleg O. Pavlov, Boris P. Yakimov

Project administration: Nastasia V. Kosheleva, Anastasia I. Shpichka, Peter S. Timashev

Resources: Peter S. Timashev

Supervision: Peter S. Timashev

Visualization: Lidiia R. Grinchevskaia, Anna V. Kardosh, Vitalia R. Izhbulatova

Writing–original draft: Lidiia R. Grinchevskaia, Anna V. Kardosh, Vitalia R. Izhbulatova

Writing–review & editing: Nastasia V. Kosheleva, Daria S. Kuznetsova, Yuri M. Efremov, Alexey L. Fayzullin, Polina Y. Bikmulina, Svetlana L. Kotova, Anastasia I. Shpichka, Peter S. Timashev

Ethics approval and consent to participate

Tissue samples were obtained from the Sechenov University Biobank; these samples were collected during tooth extraction procedures after obtaining written informed consent from healthy donors.

Consent for publication

Not applicable.

Availability of data

All the data generated or analyzed during this study are included in this published article and its supplementary information files.

Further disclosure

Part of the entire set of findings was presented at the VIII Sechenov International Biomedical Summit: Scientific and Technological Cooperation in the Medical Industry (SIBS-2024) held in Moscow, Russia, from November 6 to 7, 2024, under the title "Isolation and Characterization of Primary Human Oral Cell Cultures."

References

1. De Lauretis A, Ovrebo O, Romandini M, Lyngstadaas SP, Rossi F, Haugen HJ. From Basic Science to Clinical Practice: A Review of Current Periodontal/Mucogingival Regenerative Biomaterials. *Adv Sci*. 2024;11(17):2308848.

   doi: 10.1002/advs.202308848

2. Wolf KJ, Weiss JD, Uzel SGM, Skylar-Scott MA, Lewis JA. Biomanufacturing human tissues via organ building blocks. *Cell Stem Cell*. 2022;29(5):667-677.

   doi: 10.1016/j.stem.2022.04.012

3. Bhise NS, Manoharan V, Massa S, *et al*. A liver-on-a-chip platform with bioprinted hepatic spheroids. *Biofabrication*. 2016;8(1):014101.

   doi: 10.1088/1758-5090/8/1/014101

4. Lee J, Van Der Valk WH, Serdy SA, *et al*. Generation and characterization of hair-bearing skin organoids from human pluripotent stem cells. *Nat Protoc*. 2022;17(5):1266-1305.

   doi: 10.1038/s41596-022-00681-y

5. Birey F, Andersen J, Makinson CD, *et al*. Assembly of functionally integrated human forebrain spheroids. *Nature*. 2017;545(7652):54-59.

   doi: 10.1038/nature22330

6. Hofer M, Lutolf MP. Engineering organoids. *Nat Rev Mater*. 2021;6(5):402-420.

   doi: 10.1038/s41578-021-00279-y

7. Workman MJ, Mahe MM, Trisno S, *et al*. Engineered human pluripotent-stem-cell-derived intestinal tissues with a functional enteric nervous system. *Nat Med*. 2017;23(1):49-59.

   doi: 10.1038/nm.4233

8. Picado-Tejero D, Mendoza-Cerezo L, Rodríguez-Rego JM, Carrasco-Amador JP, Marcos-Romero AC. Recent Advances in 3D Bioprinting of Porous Scaffolds for Tissue Engineering: A Narrative and Critical Review. *J Funct Biomater*. 2025;16(9):328.

   doi: 10.3390/jfb16090328

9. Michelutti L, Tel A, Robiony M, *et al*. The Properties and Applicability of Bioprinting in the Field of Maxillofacial Surgery. *Bioengineering*. 2025;12(3):251.

   doi: 10.3390/bioengineering12030251

10. Xu H, Zhang Y, Zhang Y, *et al*. 3D bioprinting advanced biomaterials for craniofacial and dental tissue engineering – A review. *Mater Des*. 2024;241:112886.

    doi: 10.1016/j.matdes.2024.112886

11. Smirani R, Médina C, Becker J, *et al*. In vivo vessel connection of pre-vascularised 3D-bioprinted gingival connective tissue substitutes. *Biofabrication*. 2025;17(2):025009.

    doi: 10.1088/1758-5090/adac90

12. Almela T, Al-Sahaf S, Brook IM, *et al*. 3D printed tissue engineered model for bone invasion of oral cancer. *Tissue Cell*. 2018;52:71-77.

    doi: 10.1016/j.tice.2018.03.009

13. Huang GTJ, Gronthos S, Shi S. Mesenchymal Stem Cells

Derived from Dental Tissues vs. Those from Other Sources: Their Biology and Role in Regenerative Medicine. *J Dent Res*. 2009;88(9):792-806.

doi: 10.1177/0022034509340867

14. Stefańska K, Volponi AA, Kulus M, *et al*. Dental pulp stem cells – A basic research and future application in regenerative medicine. *Biomed Pharmacother*. 2024;178:116990.

doi: 10.1016/j.biopha.2024.116990

15. Miura M, Gronthos S, Zhao M, *et al*. SHED: Stem cells from human exfoliated deciduous teeth. *Proc Natl Acad Sci USA*. 2003;100(10):5807-5812.

doi: 10.1073/pnas.0937635100

16. Zhu W, Liang M. Periodontal Ligament Stem Cells: Current Status, Concerns, and Future Prospects. *Stem Cells Int*. 2015;2015:972313.

doi: 10.1155/2015/972313

17. Kang J, Fan W, Deng Q, He H, Huang F. Stem Cells from the Apical Papilla: A Promising Source for Stem Cell-Based Therapy. *Biomed Res Int*. 2019;2019:6104738.

doi: 10.1155/2019/6104738

18. Bi R, Lyu P, Song Y, et al. Function of Dental Follicle Progenitor/Stem Cells and Their Potential in Regenerative Medicine: From Mechanisms to Applications. Biomolecules. 2021;11(7):997.

doi: 10.3390/biom11070997

19. Cabaña-Muñoz ME, Pelaz Fernández MJ, Parmigiani-Cabaña JM, Parmigiani-Izquierdo JM, Merino JJ. Adult Mesenchymal Stem Cells from Oral Cavity and Surrounding Areas: Types and Biomedical Applications. *Pharmaceutics*. 2023;15(8):2109.

doi: 10.3390/pharmaceutics15082109

20. Li P, Ou Q, Shi S, Shao C. Immunomodulatory properties of mesenchymal stem cells/dental stem cells and their therapeutic applications. *Cell Mol Immunol*. 2023;20(6):558-569.

doi: 10.1038/s41423-023-00998-y

21. Awais S, Balouch SS, Riaz N, Choudhery MS. Human Dental Pulp Stem Cells Exhibit Osteogenic Differentiation Potential. *Open Life Sci*. 2020;15(1):229-236.

doi: 10.1515/biol-2020-0023

22. Sabbagh J, Ghassibe-Sabbagh M, Fayyad-Kazan M, *et al*. Differences in osteogenic and odontogenic differentiation potential of DPSCs and SHED. *J Dent*. 2020;101:103413.

doi: 10.1016/j.jdent.2020.103413

23. Li Z, Zhao Z, Gu B, *et al*. Alteration of immunomodulatory properties of locally applied gingival-derived mesenchymal stem cells by the oral inflammatory environment via Caspase-3/8 in periodontitis. *Int Immunopharmacol*. 2025;161:114978.

doi: 10.1016/j.intimp.2025.114978

24. Shetty SS, Sowmya S, Pradeep A, Jayakumar R. Gingival Mesenchymal Stem Cells: A Periodontal Regenerative Substitute. *Tissue Eng Regen Med*. 2025;22(1):1-21.

doi: 10.1007/s13770-024-00676-8

25. Cacciamali A, Villa R, Dotti S. 3D Cell Cultures: Evolution of an Ancient Tool for New Applications. *Front Physiol*. 2022;13:836480.

doi: 10.3389/fphys.2022.836480

26. Ji Q, Tang R, Liu X, *et al*. From microtissues to organs: the future of reconstructive surgery with organ building block-based bioprinting. *Biofabrication*. 2025;17(3):032010.

doi: 10.1088/1758-5090/aded37

27. Bikmulina P, Kosheleva N, Efremov Y, *et al*. 3D or not 3D: a guide to assess cell viability in 3D cell systems. *Soft Matter*. 2022;18(11):2222-2233.

doi: 10.1039/D2SM00018K

28. Dominici M, Le Blanc K, Mueller I, *et al*. Minimal criteria for defining multipotent mesenchymal stromal cells. The International Society for Cellular Therapy position statement. *Cytotherapy*. 2006;8(4):315-317.

doi: 10.1080/14653240600855905

29. Fonseca LN, Bolívar-Moná S, Agudelo T, *et al*. Cell surface markers for mesenchymal stem cells related to the skeletal system: A scoping review. *Heliyon*. 2023;9(2):e13464.

doi: 10.1016/j.heliyon.2023.e13464

30. Lertkiatmongkol P, Liao D, Mei H, Hu Y, Newman PJ. Endothelial functions of platelet/endothelial cell adhesion molecule-1 (CD31). *Curr Opin Hematol*. 2016;23(3):253-259.

doi: 10.1097/MOH.0000000000000239

31. Huang MS, Christakopoulos F, Roth JG, Heilshorn SC. Organoid bioprinting: from cells to functional tissues. *Nat Rev Bioeng*. 2025;3(2):126-142.

doi: 10.1038/s44222-024-00268-0

32. Kuntjoro M, Hendrijantini N, Agustono B, Rahmania PN, Al Bana FR, Gabriela N. Osteogenic differentiation enhancement of human dental pulp mesenchymal stem cells: A review. *World J Adv Res Rev*. 2023;19(2):146-151.

doi: 10.30574/wjarr.2023.19.2.1525

33. Nowwarote N, Petit S, Ferre FC, *et al*. Extracellular Matrix Derived From Dental Pulp Stem Cells Promotes Mineralization. *Front Bioeng Biotechnol*. 2022;9:740712.

doi: 10.3389/fbioe.2021.740712

34. Kornsuthisopon C, Nowwarote N, Chansaenroj A, *et al*. Human dental pulp stem cells derived extracellular matrix

promotes mineralization via Hippo and Wnt pathways. *Sci Rep*. 2024;14(1):6777.

doi: 10.1038/s41598-024-56845-1

35. Martinez EF, Araújo VC. In vitro immunoexpression of extracellular matrix proteins in dental pulpal and gingival human fibroblasts. *Int Endod J*. 2004;37(11):749-755.

doi: 10.1111/j.1365-2591.2004.00864.x

36. Angelopoulos I, Brizuela C, Khoury M. Gingival Mesenchymal Stem Cells Outperform Haploidentical Dental Pulp-derived Mesenchymal Stem Cells in Proliferation Rate, Migration Ability, and Angiogenic Potential. *Cell Transplant*. 2018;27(6):967-978.

doi: 10.1177/0963689718759649

37. Roato I, Chinigò G, Genova T, Munaron L, Mussano F. Oral Cavity as a Source of Mesenchymal Stem Cells Useful for Regenerative Medicine in Dentistry. *Biomedicines*. 2021;9(9):1085.

doi: 10.3390/biomedicines9091085

38. Lee H, Hwa S, Cho S, *et al*. Impact of Polydeoxyribonucleotides on the Morphology, Viability, and Osteogenic Differentiation of Gingiva-Derived Stem Cell Spheroids. *Medicina*. 2024;60(10):1610.

doi: 10.3390/medicina60101610

39. Toyoda M, Fukuda T, Fujimoto R, *et al*. Scaffold-free bone-like 3D structure established through osteogenic differentiation from human gingiva-derived stem cells. *Biochem Biophys Rep*. 2024;38:101656.

doi: 10.1016/j.bbrep.2024.101656

40. Alfonso García SL, Mira Uribe LM, Castaño López S, Parada-Sanchez MT, Arboleda-Toro D. Ultrastructural Characterization of Human Gingival Fibroblasts in 3D Culture. *Cells*. 2022;11(22):3647.

doi: 10.3390/cells11223647

41. Guo L, Zou Z, Freytag M, *et al*. Human Dental Pulp Cells form Spheroids in the Presence of Serum When Seeded on a Low-Attachment Cultural Surface. *Processes*. 2022;10(5):1021.

doi: 10.3390/pr10051021

42. Zheng Y, Jiang L, Yan M, *et al*. Optimizing Conditions for Spheroid Formation of Dental Pulp Cells in Cell Culture. *In Vivo*. 2021;35(4):1965-1972.

doi: 10.21873/invivo.12464

43. Liu F, Wu Q, Liu Q, *et al*. Dental pulp stem cells-derived cannabidiol-treated organoid-like microspheroids show robust osteogenic potential via upregulation of WNT6. *Commun Biol*. 2024;7(1):972.

doi: 10.1038/s42003-024-06655-y

44. Van Der Geest AT, Jakobs CE, Ljubikj T, *et al*. Molecular pathology, developmental changes and synaptic dysfunction in (pre-) symptomatic human C9ORF72-ALS/FTD cerebral organoids. *Acta Neuropathol Commun*. 2024;12(1):152.

doi: 10.1186/s40478-024-01857-1

45. Yin J, VanDongen AM. Enhanced Neuronal Activity and Asynchronous Calcium Transients Revealed in a 3D Organoid Model of Alzheimer's Disease. *ACS Biomater Sci Eng*. 2021;7(1):254-264.

doi: 10.1021/acsbiomaterials.0c01583

46. Kronemberger GS, Spagnuolo FD, Karam AS, Chattahy K, Storey KJ, Kelly DJ. Rapidly Degrading Hydrogels to Support Biofabrication and 3D Bioprinting Using Cartilage Microtissues. *ACS Biomater Sci Eng*. 2024;10(10):6441-6450.

doi: 10.1021/acsbiomaterials.4c00819

47. Tartagni O, Borók A, Mensà E, *et al*. Microstructured soft devices for the growth and analysis of populations of homogenous multicellular tumor spheroids. *Cell Mol Life Sci*. 2023;80(4):93.

doi: 10.1007/s00018-023-04748-1

48. Kosheleva NV, Efremov YM, Koteneva PI, *et al*. Building a tissue: Mesenchymal and epithelial cell spheroids mechanical properties at micro- and nanoscale. *Acta Biomater*. 2023;165:140-152.

doi: 10.1016/j.actbio.2022.09.051

49. Revokatova DP, Koteneva PI, Kosheleva NV, Shpichka AI, Timashev PS. Spheroids from Epithelial and Mesenchymal Cell Phenotypes as Building Blocks in Bioprinting (Review). *Sovrem Tekhnol Med*. 2025;17(1):121-132.

doi: 10.17691/stm2025.17.1.11

50. Rovere M, Reverberi D, Arnaldi P, Palamà MEF, Gentili C. Spheroid size influences cellular senescence and angiogenic potential of mesenchymal stromal cell-derived soluble factors and extracellular vesicles. *Front Bioeng Biotechnol*. 2023;11:1297644.

doi: 10.3389/fbioe.2023.1297644

51. Nilsson Hall G, Rutten I, Lammertyn J, *et al*. Cartilaginous spheroid-assembly design considerations for endochondral ossification: towards robotic-driven biomanufacturing. *Biofabrication*. 2021;13(4):045025.

doi: 10.1088/1758-5090/ac2208

52. Efremov YM, Zurina IM, Presniakova VS, *et al*. Mechanical properties of cell sheets and spheroids: the link between single cells and complex tissues. *Biophys Rev*. 2021;13(4):541-561.

doi: 10.1007/s12551-021-00821-w

53. Banerjee D, Singh YP, Datta P, *et al*. Strategies for 3D bioprinting of spheroids: A comprehensive

review. *Biomaterials*. 2022;291:121881.

doi: 10.1016/j.biomaterials.2022.121881

54. De Moor L, Fernandez S, Vercruysse C, *et al*. Hybrid Bioprinting of Chondrogenically Induced Human Mesenchymal Stem Cell Spheroids. *Front Bioeng Biotechnol*. 2020;8:484.

doi: 10.3389/fbioe.2020.00484

55. Bikmulina P, Kosheleva N, Efremov Y, *et al*. Building a tissue: gingiva- and adipose-derived mesenchymal cell spheroids' survivability and functionality after 3D extrusion bioprinting. *Bioprinting*. 2023;32:e00279.

doi: 10.1016/j.bprint.2023.e00279

56. Skala MC, Riching KM, Bird DK, *et al*. In vivo multiphoton fluorescence lifetime imaging of protein-bound and free nicotinamide adenine dinucleotide in normal and precancerous epithelia. *J Biomed Opt*. 2007;12(2):024014.

doi: 10.1117/1.2717503

57. Stringari C, Edwards RA, Pate KT, Waterman ML, Donovan PJ, Gratton E. Metabolic trajectory of cellular differentiation in small intestine by Phasor Fluorescence Lifetime Microscopy of NADH. *Sci Rep*. 2012;2(1):568.

doi: 10.1038/srep00568

58. Heikal AA. Intracellular Coenzymes as Natural Biomarkers for Metabolic Activities and Mitochondrial Anomalies. *Biomark Med*. 2010;4(2):241-263.

doi: 10.2217/bmm.10.1